Propulsion Theory of Flapping Airfoils, Comparison with Computational Fluid Dynamics

D. F. Hunsaker* and W. F. Phillips†
Utah State University, Logan, Utah 84322-4130

It is shown that the time-dependent aerodynamic forces acting on a flapping airfoil in forward flight are functions of both axial and normal reduced frequencies. The axial reduced frequency is based on the chord length and the normal reduced frequency is based on the plunging amplitude. Furthermore, the time-dependent aerodynamic forces are related to two Fourier coefficients, which are evaluated here from computational results. Correlation equations for these Fourier coefficients are obtained from a large number of grid- and time-step-resolved inviscid computational fluid dynamics solutions, conducted over a range of both axial and normal reduced frequencies. The correlation results can be used to predict the thrust, required power, and propulsive efficiency for airfoils in forward flight with sinusoidal pitching and plunging motion. Within the range of parameters typically encountered in the efficient forward flight of birds, results obtained from the correlation equations match the computational fluid dynamics results more closely than do those obtained from the classical Theodorsen model.

Nomenclature

A = Fourier coefficient defined in Eq. (13)

A_{x0-x2} = coefficients defined in Eq. (14)

A_{y1} = coefficient defined in Eq. (15)

A_{12-32} = correlation coefficients used in Eq. (28) and defined in Table 1

B = Fourier coefficient defined in Eq. (13)

B_{x1-x2} = coefficients defined in Eq. (14)

B_{y1} = coefficient defined in Eq. (15)

* Assistant Professor, Mechanical and Aerospace Engineering Department, 4130 Old Main Hill. Member AIAA.
† Emeritus Professor, Mechanical and Aerospace Engineering Department, 4130 Old Main Hill. Senior Member AIAA.

$B_{12–30}$ = correlation coefficients used in Eq. (29) and defined in Table 1

C_L, $\overline{C}_L$ = instantaneous and mean section lift coefficients

$\widetilde{C}_{L,\alpha}$ = airfoil-section lift slope

$C_{m_{ac}}$ = section pitching-moment coefficient about the airfoil aerodynamic center

C_P, $\overline{C}_P$ = instantaneous and mean section required-power coefficients

C_x, $\overline{C}_x$ = instantaneous and mean section axial-force coefficients

C_y = section normal-force coefficient

$C_{0–\infty}$ = coefficients in the Taylor series expansion given in Eq. (11)

c = airfoil section chord length

F_x = section axial force

F_y = section normal force

k = reduced frequency used by Theodorsen based on the airfoil half chord $k \equiv \omega c/(2V_\infty)$

m_{ac} = section pitching moment about the airfoil aerodynamic center

R_{y1} = amplitude of the sinusoidal terms A_{y1} and B_{y1}

$T_{A1–2}$ = correlation coefficients used in Eq. (28) and defined in Table 1

$T_{B1–2}$ = correlation coefficients used in Eq. (29) and defined in Table 1

t = time

V_∞ = freestream airspeed

V_y = y-velocity component of the airfoil aerodynamic center (positive upward)

x, y, z = streamwise, upward normal, and spanwise coordinates relative to the section aerodynamic center

y_A = aerodynamic-center plunging amplitude

y_{ac} = aerodynamic-center plunging displacement

α, $\overline{\alpha}$ = instantaneous and mean pitching angles

$\dot{\alpha}$ = pitching angular velocity

α_A = pitching amplitude

α_g = geometric angle of attack

α_i = induced angle of attack

α_{L0} = zero-lift angle of attack

$\hat{\alpha}_y$ = aerodynamic-center geometric angle-of-attack ratio defined in Eq. (6)

η = propulsive efficiency

φ_{y1} = phase shift of the sinusoidal terms A_{y1} and B_{y1}

λ = wave length for the trailing vortex wake

ρ = fluid density

τ = flapping period

ω = flapping frequency

$\hat{\omega}_x$ = reduced frequency based on the airfoil chord and defined in Eq. (21)

$\hat{\omega}_y$ = reduced frequency based on the aerodynamic-center plunging amplitude and defined in Eq. (5)

I. Introduction

The lift from a plunging airfoil in forward flight is rotated forward through an incremental angle of attack, which, within the small-angle approximation, is proportional to the plunging velocity. The rotation of the lift vector through this angle results in the production of thrust. Low-frequency two-dimensional quasi-steady effects of the physics for the production of thrust by a flapping airfoil in forward flight were presented first by Knoller [1], and independently by Betz [2]. A decade later, Katzmayr [3] demonstrated the production of thrust experimentally using the Knoller–Betz low-frequency flapping-airfoil model.

Aerodynamic forces and moments acting on an airfoil in oscillatory motion are affected by the oscillating vortex wake downstream from the airfoil. The oscillating vorticity in the wake induces fluid motion near the airfoil, which alters the pressure distribution acting on the airfoil relative to that experienced in steady flow. At low frequencies, this effect is small. However, at higher frequencies, the influence of the oscillating wake on the aerodynamics of the airfoil is significant. The foundation for much of the analytical work on oscillating airfoils in forward flight can be traced back to the work of Wagner [4], who calculated the vorticity in the wake of an airfoil with non-uniform motion. A few years later, Glauert [5] was among the first to develop relations for the lift and pitching moment acting on an oscillating airfoil. A review of Glauert's work was presented by von Kármán and Burgers [6] who added an analytical expression for the propulsive force developed by the airfoil.

Theodorsen [7] developed an analytical model for oscillating airfoils in forward flight based on conformal mapping, and he presented expressions for the lift and pitching moment acting on an airfoil with three degrees of freedom. However, because his work was focused on understanding the mechanism of flutter, Theodorsen omitted the calculation of the force in the streamwise direction. Later, Garrick [8] used Theodorsen's mathematical model to extend the work of von Kármán and Burgers [6] to an airfoil with three degrees of freedom, and he presented expressions for the axial force and propulsive efficiency of a flapping airfoil. Theodorsen's [7] mathematical model with Garrick's [8] extension has been widely used to predict the aerodynamics of flapping airfoils in forward flight.

The approximations underlying Theodorsen's [7] potential-flow solution include those of a thin airfoil with small camber, small angles of attack, small-amplitude sinusoidal oscillations, and a planar wake with oscillating vorticity. As with the aerodynamic theory of steady flow, analytical results based on these seemingly constraining

approximations often give reasonable results well outside the range of parameters for which these approximations might be expected to hold. However, it is important to note that the assumptions used by Theodorsen resulted in a wake model dependent on a single reduced frequency. Traditionally, the term *reduced frequency* is used to denote a dimensionless parameter defined to be the product of a frequency and a characteristic length divided by the freestream airspeed. Theodorsen defined the parameter, k, as the axial reduced frequency and used one-half the chord length as the characteristic length. Hence, much of the subsequent flapping-flight work has been presented in terms of this single reduced frequency, k.

It can be analytically shown that Theodorsen's [7] model exhibits the correct asymptotic behavior at low flapping frequencies. However, in the high-frequency limit, Theodorsen's model predicts infinite amplitude oscillations in the aerodynamic forces and moments at finite geometric pitching and plunging angle-of-attack amplitudes, which is clearly unrealistic [9]. For a review of this model as well as a presentation of the model using modern conventional notation, the reader is referred to Hunsaker and Phillips [9].

Recently, most investigations of airfoil flapping have focused on experimental studies [10,11] and numerical solutions that use either potential-flow theory [12,13] or computational fluid dynamics (CFD) [14,15]. Because the Theodorsen [7] model appears to be applicable over the range of frequencies and amplitudes that are of interest in efficient flapping flight, this model is often used for comparison in CFD and experimental studies [15,16,17], which show varying degrees of agreement with the Theodorsen model.

An alternate approach to that taken by Theodorsen [7] for predicting the aerodynamics of a flapping airfoil is to use numerical solutions or experimental data to calibrate the frequency dependence of the unsteady aerodynamic coefficients. Such an approach may be better suited for modeling the propulsion of flapping airfoils at high flapping frequencies where Theodorsen's model is less accurate. In this study, inviscid CFD solutions are obtained over a range of frequencies and amplitudes typically encountered in the efficient forward flight of birds. The results are correlated to produce algebraic relations that can be used to predict the thrust, required power, and propulsive efficiency of flapping airfoils over a wide range of flapping frequencies and amplitudes. Results from the classical Theodorsen model are also included for comparison.

II. Two-Dimensional Small-Angle Sinusoidal Plunging and Pitching

Consider a 2-dimensional airfoil section immersed in a uniform flow with a constant freestream velocity, V_∞, as shown schematically in Fig. 1. The airfoil is undergoing sinusoidal vertical displacement, $y_{ac}(t)$, of its aerodynamic center combined with small-angle sinusoidal rotation, $\alpha(t)$, about its aerodynamic center. The displacement y_{ac} has a zero mean and is positive upward, the rotation α has a mean value of $\overline{\alpha}$ and is positive clockwise relative to the constant freestream velocity, which approaches the airfoil from the left.

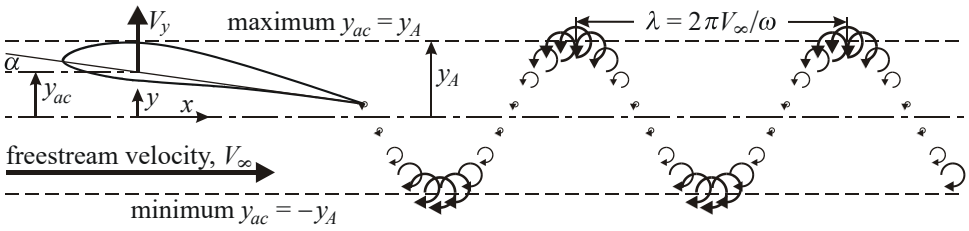

Figure 1. Parameters used to describe the combined plunging and pitching motion.

(Note to the Copy Editor: Because of the figure aspect ratio, this figure was designed as a two-column figure. The Associate Editor asked us to add this figure and we were unable to convey the required information in a single-column figure.)

For this motion, the position of the airfoil's aerodynamic center in the direction normal to the freestream velocity can be expressed in terms of an amplitude, y_A, and a frequency, ω, i.e.,

$$y_{ac}(t) = y_A \sin(\omega t) \tag{1}$$

Hence, the upward normal-velocity component of the airfoil's aerodynamic center is

$$V_y(t) = \omega y_A \cos(\omega t) \tag{2}$$

Here we shall consider the case when the pitching angle, $\alpha(t)$, is oscillating at the same frequency and is in phase with the upward y-velocity component, $V_y(t)$. Denoting the pitching amplitude as α_A, we have

$$\alpha(t) = \overline{\alpha} + \alpha_A \cos(\omega t) \tag{3}$$

Using the small-angle approximation, the total geometric angle of attack is then

$$\alpha_g(t) = \overline{\alpha} - \hat{\omega}_y(1-\hat{\alpha}_y)\cos(\omega t) \tag{4}$$

where $\hat{\omega}_y$ and $\hat{\alpha}_y$ are defined as

$$\hat{\omega}_y \equiv \omega y_A / V_\infty \tag{5}$$

$$\hat{\alpha}_y \equiv \alpha_A / \hat{\omega}_y \tag{6}$$

Note that $\hat{\omega}_y$ is a reduced frequency similar to Theodorsen's [7] reduced frequency, k, except that $\hat{\omega}_y$ is based on the plunging amplitude, y_A, whereas Theodorsen's reduced frequency was based on the airfoil section half-chord length. From Eq. (2), it can be seen that $\hat{\omega}_y$ is also the small-angle geometric angle-of-attack amplitude due to plunging, i.e., amplitude$[V_y(t)/V_\infty]$. Also notice that $\hat{\alpha}_y$ is a geometric angle-of-attack ratio at the airfoil aerodynamic center. It is simply the ratio of the amplitude due to pitching to that due to plunging. Because thrust is produced only by plunging, for efficient forward flight, $\hat{\alpha}_y$ is typically small.

The oscillating airfoil creates an oscillating vortex wake downstream from the airfoil, as shown schematically in Fig. 1. In order to help visualize the vorticity and shape of the trailing wake, the wake in this figure is compressed along the *x* axis. For high-speed forward flight, the ratio of the wave length λ to the airfoil chord length *c* would be much greater than that shown in Fig. 1. The flapping period is $\tau = 2\pi/\omega$ and the wake is carried downstream at the velocity V_∞. Hence, the wave length can be written in dimensionless form as $\lambda/c = 2\pi V_\infty/(\omega c)$. For birds in efficient forward flight, the wave length is typically in the range $15 < \lambda/c < 210$. Whereas Theodorsen assumed a planar wake, here we make no assumptions as to the wake shape, but instead assume that the effects of the wake can be included through a time-dependent induced angle of attack, $\alpha_i(t)$.

Assuming a linear relation between the lift coefficient and the total airfoil angle of attack, the lift coefficient can be written in terms of the airfoil section lift slope $\widetilde{C}_{L,\alpha}$, total geometric angle of attack $\alpha_g(t)$, induced angle of attack $\alpha_i(t)$, and the zero-lift angle of attack α_{L0} as

$$C_L(t) \;=\; \widetilde{C}_{L,\alpha}[\alpha_g(t) + \alpha_i(t) - \alpha_{L0}] \tag{7}$$

or after applying Eq. (4),

$$C_L(t) \;=\; \widetilde{C}_{L,\alpha}[\overline{\alpha} - \hat{\omega}_y(1-\hat{\alpha}_y)\cos(\omega t) + \alpha_i(t) - \alpha_{L0}] \tag{8}$$

The lift vector is perpendicular to the relative wind. Hence, it is rotated through the angle of attack due to plunging, $-\hat{\omega}_y \cos(\omega t)$, and the induced angle of attack, $\alpha_i(t)$. However, it is not rotated through the angle of attack due to pitching. Within the small-angle approximation, the axial and normal components of lift are

$$C_x(t) \;=\; -\widetilde{C}_{L,\alpha}[\overline{\alpha} - \hat{\omega}_y(1-\hat{\alpha}_y)\cos(\omega t) + \alpha_i(t) - \alpha_{L0}][-\hat{\omega}_y \cos(\omega t) + \alpha_i(t)] \tag{9}$$

$$C_y(t) \;=\; C_L(t) \;=\; \widetilde{C}_{L,\alpha}[\overline{\alpha} - \hat{\omega}_y(1-\hat{\alpha}_y)\cos(\omega t) + \alpha_i(t) - \alpha_{L0}] \tag{10}$$

In general, the instantaneous induced angle of attack could depend on the oscillating component of the geometric angle of attack and all of its time derivatives, i.e.,

$$\alpha_i(t) \;=\; C_0[\alpha_g(t) - \overline{\alpha}] + \sum_{n=1}^{\infty} C_n \frac{d^n \alpha_g}{dt^n} \tag{11}$$

The time derivatives of the geometric angle of attack can be evaluated from Eq. (4), which gives

$$\frac{d^n \alpha_g}{dt^n} \;=\; \hat{\omega}_y(1-\hat{\alpha}_y) \begin{cases} (-1)^{(n+3)/2}\,\omega^n \sin(\omega t), \text{ for } n \text{ odd} \\ (-1)^{(n+2)/2}\,\omega^n \cos(\omega t), \text{ for } n \text{ even} \end{cases} \tag{12}$$

Using Eqs. (4) and (12) in Eq. (11) yields

$$\alpha_i(t) \;=\; \hat{\omega}_y(1-\hat{\alpha}_y)[A\cos(\omega t)+B\sin(\omega t)],\;\text{ where}$$
$$A \;\equiv\; \sum_{\substack{n=0\\ n\,\text{even}}}^{\infty}(-1)^{(n+2)/2}C_n\,\omega^n, \quad B \;\equiv\; \sum_{\substack{n=1\\ n\,\text{odd}}}^{\infty}(-1)^{(n+3)/2}C_n\,\omega^n \tag{13}$$

Note that the Fourier coefficients A and B in Eq. (13) depend on the sinusoidal frequency. Furthermore, the coefficients C_n could depend on the frequency and other flow-field variables, such as the freestream velocity, airfoil chord length, and the plunging and pitching amplitudes. However, for this steady sinusoidal plunging and pitching, the coefficients A and B do not vary with time over the flapping cycle.

Applying the trigonometric identities $\cos^2\theta=[1+\cos(2\theta)]/2$, $\sin^2\theta=[1-\cos(2\theta)]/2$, and $\cos\theta\sin\theta=\sin(2\theta)/2$, while using Eq. (13) in Eqs. (9) and (10), the instantaneous axial- and normal-force coefficients are found to be

$$\begin{aligned} C_x(t) \;&=\; \overline{C}_L\,\hat{\omega}_y[A_{x1}\cos(\omega t)+B_{x1}\sin(\omega t)]-\widetilde{C}_{L,\alpha}\,\hat{\omega}_y^2(1-\hat{\alpha}_y)[A_{x0}+A_{x2}\cos(2\omega t)+B_{x2}\sin(2\omega t)] \\ A_{x0} &\equiv [(1-A)(1-A+\hat{\alpha}_y A)+(1-\hat{\alpha}_y)B^2]\big/2, \quad A_{x1} \equiv 1-(1-\hat{\alpha}_y)A, \quad B_{x1} \equiv -(1-\hat{\alpha}_y)B, \\ A_{x2} &\equiv [(1-A)(1-A+\hat{\alpha}_y A)-(1-\hat{\alpha}_y)B^2]\big/2, \quad B_{x2} \equiv -[(1-A)(1-\hat{\alpha}_y)+\hat{\alpha}_y/2]B \end{aligned} \tag{14}$$

$$\begin{aligned} C_y(t) \;&=\; \overline{C}_L-\widetilde{C}_{L,\alpha}\,\hat{\omega}_y(1-\hat{\alpha}_y)[A_{y1}\cos(\omega t)+B_{y1}\sin(\omega t)] \\ A_{y1} &\equiv 1-A, \quad B_{y1} \equiv -B \end{aligned} \tag{15}$$

where the mean lift coefficient is

$$\overline{C}_L \;=\; \widetilde{C}_{L,\alpha}(\overline{\alpha}-\alpha_{L0}) \tag{16}$$

Integrating Eq. (14) over one cycle and dividing by the period, $\tau=2\pi/\omega$, the mean axial-force coefficient is

$$\overline{C}_x \;\equiv\; \frac{1}{\tau}\int_{t=0}^{\tau}C_x(t)dt \;=\; -\widetilde{C}_{L,\alpha}\,\hat{\omega}_y^2(1-\hat{\alpha}_y)[(1-A)(1-A+\hat{\alpha}_y A)+(1-\hat{\alpha}_y)B^2]\big/2 \tag{17}$$

Each pair of sinusoidal terms in Eqs. (14) and (15) can be written in terms of an amplitude and phase. For example, the pair of sinusoidal terms in Eq. (15) can be written as

$$A_{y1}\cos(\omega t)+B_{y1}\sin(\omega t) \;=\; R_{y1}\cos(\omega t+\varphi_{y1}) \tag{18}$$

where

$$R_{y1} \;=\; \sqrt{A_{y1}^2+B_{y1}^2} \;=\; \sqrt{(1-A)^2+B^2} \tag{19}$$

$$\varphi_{y1} \;=\; \tan^{-1}(-B_{y1}/A_{y1}) \;=\; \tan^{-1}[B/(1-A)] \tag{20}$$

Notice from Eqs. (13)–(15) that the 7 coefficients, A_{x0}, A_{x1}, B_{x1}, A_{x2}, B_{x2}, A_{y1}, and B_{y1}, depend on the plunging frequency. However, for steady sinusoidal oscillations, these are Fourier coefficients that do not vary with time over the flapping cycle. It should also be noted that, within the small-angle approximation, the normal-force coefficient varies sinusoidally with time at the plunging frequency, but is phase shifted relative to the plunging cycle. The temporal variation in the axial-force coefficient oscillates with only the plunging frequency and its first harmonic, both of which are phase shifted relative to the plunging cycle.

From Eqs. (14) and (15), we see that the axial- and normal-force coefficients depend on at least one important reduced frequency, $\hat{\omega}_y$, which was defined in Eq. (5). The ratio of the wave length λ, which is shown schematically in Fig. 1, to the airfoil chord length c can be written as $\lambda/c = 2\pi V_\infty/(\omega c)$. Hence, we should expect the axial- and normal-force coefficients to depend on two reduced frequencies, i.e., the normal reduced frequency, $\hat{\omega}_y$, and an axial reduced frequency,

$$\hat{\omega}_x \equiv \omega c/V_\infty \tag{21}$$

The reduced frequency $\hat{\omega}_y$ appears naturally in the formulation presented here. The reduced frequency $\hat{\omega}_x$ affects the solution through its effect on the wave length of the trailing vortex sheet. Because the induced angle of attack depends on the variation in the strength of the trailing vortex sheet with the axial coordinate, we should expect the Fourier coefficients A and B, defined in Eq. (13), to be strong functions of $\hat{\omega}_x$. Note that $\hat{\omega}_x$ is simply twice the reduced frequency introduced by Theodorsen [7], ie., $\hat{\omega}_x = 2k$. This is because we have chosen the chord length as the axial length scale, whereas Theodorsen's [7] reduced frequency was based on the half-chord length.

For the special case of quasi-steady sinusoidal oscillations, the axial reduced frequency $\hat{\omega}_x$, the induced angle of attack α_i, and the Fourier coefficients A and B all approach zero. Hence, the 7 Fourier coefficients in Eqs. (14) and (15) reduce to the low-frequency limit

$$A_{x0} = 1/2, \quad A_{x1} = 1, \quad B_{x1} = 0, \quad A_{x2} = 1/2, \quad B_{x2} = 0, \quad A_{y1} = 1, \quad B_{y1} = 0$$

The traditional coefficient for the instantaneous power required to support this pitching and plunging motion is

$$C_P(t) \equiv \frac{-F_y(t)V_y(t) - m_{ac}\dot{\alpha}(t)}{\frac{1}{2}\rho V_\infty^3 c} = \frac{-C_y(t)V_y(t) - C_{m_{ac}} c\dot{\alpha}(t)}{V_\infty}$$

Within the small-angle approximation, for the special case when the pitching angle is in phase with the upward y-velocity component of the airfoil's aerodynamic center, after applying Eqs. (2), (3), (5), (6), (15), and (21), the coefficient for the instantaneous required power is obtained from the relation

$$C_P(t) = -\{\overline{C}_L \hat{\omega}_y - \widetilde{C}_{L,\alpha}\hat{\omega}_y^2(1-\hat{\alpha}_y)[(1-A)\cos(\omega t) - B\sin(\omega t)]\}\cos(\omega t) + C_{m_{ac}}\hat{\omega}_x\hat{\omega}_y\hat{\alpha}_y \sin(\omega t) \tag{22}$$

Integrating Eq. (22) over one cycle and dividing by the period, $\tau = 2\pi/\omega$, the mean required-power coefficient is

$$\overline{C}_P \equiv \frac{1}{\tau}\int_{t=0}^{\tau} C_P(t)dt = \widetilde{C}_{L,\alpha}\,\hat{\omega}_y^2(1-\hat{\alpha}_y)(1-A)/2 \tag{23}$$

The instantaneous available propulsive power is the negative of the x component of the aerodynamic force acting on the airfoil, F_x, multiplied by the forward airspeed, V_∞. Hence, the traditional aerodynamic coefficient for the available propulsive power is simply

$$\frac{-F_x V_\infty}{\frac{1}{2}\rho V_\infty^3 c} = -C_x(t) \tag{24}$$

The propulsive efficiency is the mean available propulsive power divided by the mean required power. Hence, in view of Eqs. (17), (23), and (24), for the special case when the pitching angle is in phase with the upward y-velocity component of the airfoil's aerodynamic center, the propulsive efficiency is given by

$$\eta = -\overline{C}_x/\overline{C}_P = 1-(1-\hat{\alpha}_y)[A-B^2/(1-A)] \tag{25}$$

In order to predict the time-dependent wake-induced angle of attack and its effect on the airfoil forces, we must obtain values for the Fourier coefficients A and B, which were introduced in Eq. (13). However, because A and B depend on the coefficients C_n, which are not known a priori, analytical solutions for the Fourier coefficients A and B are difficult, if not impossible, to develop. Notice from Eq. (23) that, within the small-angle approximation, the mean required power is independent of the Fourier coefficient B. Hence, if the mean required-power coefficient is somehow determined for a given set of operating conditions, the corresponding Fourier coefficient A can be evaluated from Eq. (23), i.e.,

$$A = 1-\frac{2\overline{C}_P}{\widetilde{C}_{L,\alpha}\,\hat{\omega}_y^2(1-\hat{\alpha}_y)} \tag{26}$$

Furthermore, if the mean axial-force coefficient is similarly determined, the Fourier coefficient B can be evaluated from Eq. (17) and the known value of A that was obtained from the power coefficient using Eq. (26). This gives

$$B = \sqrt{\frac{-2\overline{C}_x}{\widetilde{C}_{L,\alpha}\,\hat{\omega}_y^2(1-\hat{\alpha}_y)^2} - \frac{(1-A)(1-A+\hat{\alpha}_y A)}{(1-\hat{\alpha}_y)}} \tag{27}$$

Once the Fourier coefficients A and B have been determined from Eqs. (26) and (27), the temporal variation in the wake-induced angle of attack can be obtained from Eq. (13).

In the research study reported here, the mean required-power and axial-force coefficients were evaluated for a wide range of operating conditions from inviscid CFD solutions. These solutions were used with Eqs. (26) and (27)

to evaluate the Fourier coefficients A and B and the results were used to obtain algebraic correlation equations, which relate A and B to the nondimensional operating parameters $\hat{\omega}_x$, $\hat{\omega}_y$, and $\hat{\alpha}_y$.

III. Inviscid Computational Fluid Dynamics Solutions

All CFD solutions were obtained using version 8.06 of the commercially available software Star-CCM+ [18] This software is capable of solving the three-dimensional, time-dependent, Reynolds-averaged, Navier–Stokes equations using a finite-volume formulation on an unstructured grid. However, to be consistent with potential flow theory upon which Theodorsen's [7] model is based, the available inviscid solver was used for this study. Unsteady, incompressible computations were performed using the segregated flow solver. Second-order upwinding was used for the convection terms and the implicit unsteady solver was used with second-order temporal discretization. Constant fluid density of 1.225 kg/m^3 and a freestream velocity of 14 m/s were used for all computations, which gives a freestream Mach number of 0.041. A von Kármán Trefftz airfoil with a maximum thickness of 15%, a chord length of 0.25 m, and a zero-lift angle of attack of −5.0 degrees was used for these computations. The geometry of a von Kármán Trefftz airfoil can be completely defined from its thickness, chord length, and zero-lift angle of attack. This airfoil was chosen because conformal mapping provides an exact potential-flow solution for steady flow. This solution was used to evaluate the error in the grid convergence study. The analytical aerodynamic center is located at $x/c = 0.2757$ and $y/c = 0.0061$, and the analytical pitching moment about the aerodynamic center is −0.1296. The airfoil lift slope is 7.0361. For further details on conformal mapping and the von Kármán Trefftz family of airfoils, see for example Karamcheti [19].

The time-dependent motion of the airfoil was modeled using an overset grid that moved relative to a fixed background grid. The overset grid translated vertically according to the aerodynamic-center plunging motion given in Eq. (1), $y_A \sin(\omega t)$, while rotating about the airfoil aerodynamic center according to the pitching motion given in Eq. (3) with $\overline{\alpha} = 0$, $\alpha_A \cos(\omega t)$. The pitching and plunging motions were specified by the pitching and plunging velocities, which were integrated by the software to evaluate the position and orientation as a function of time.

A structured C-grid was used for both the overset and background grids. Nodes were clustered near the leading and trailing edges of the airfoil and in the wake region aft of the airfoil to improve accuracy and provide improved resolution of the oscillating wake [20]. The C-portion of the background grid was set as a velocity inlet boundary, the exit plane was set as a flow-split outlet with a split ratio of 1.0, and a slip boundary condition was specified on the airfoil surface. Two-dimensional airfoil results were obtained from the three-dimensional solver by using three identical grid planes in the z-direction, and setting the two outboard z-planes to symmetry boundary conditions.

To evaluate grid convergence, three similar grids were generated from an initial fine background grid. A medium background grid was created by removing every other node from the fine grid, and a coarse background

grid was created by removing every other node from the medium grid. The overset grid was generated by removing several outer circumferential layers from the background grid. A sample coarse grid is shown in Fig. 2.

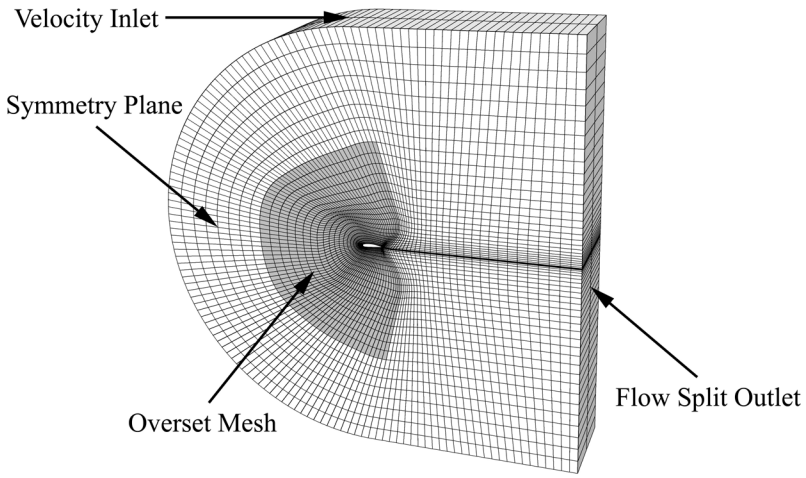

Figure 2. Example coarse grid for computational fluid dynamics calculations.

To evaluate the accuracy of solutions obtained from a given grid, results from a series of steady-flow cases representing 16 steps in a quasi-steady flapping cycle were compared with the analytical solution for the airfoil forces and pitching moment. For each case, the freestream angle of attack was set to zero, the overset grid was offset relative to the background grid according to the translation specified by Eq. (1), $y_A \sin(\omega t)$, and the overset grid was given a steady translational velocity specified by Eq. (2), $\omega y_A \cos(\omega t)$. This created a steady-state case at the same vertical offset and geometric angle of attack as the airfoil would experience at that point in the transient simulations. Because inviscid CFD computations usually produce flow separation at lower angles of attack than are observed experimentally, values for y_A and ω used for this grid convergence study were chosen to give geometric angles of attack ranging from –4.0 to 4.0 degrees. This gives a range in the analytical lift coefficient from 0.1232 to 1.104. The grid was refined and the size of the overset grid was varied to reduce the CFD error, relative to the analytical solutions, to an acceptable level. These grid refinement studies resulted in a final fine background grid with 561 circumferential nodes and 121 radial nodes (67,200 cells per plane) and an overset grid with 337 circumferential nodes and 89 radial nodes (29,568 cells per plane). This grid will be referred to here as the *fine grid*.

Figures 3–5 show typical results for the lift, drag, and aerodynamic-center pitching-moment coefficients for the final coarse, medium, and fine grids compared to the analytical solutions in the angle-of-attack range from –4.0 to 4.0 degrees. The fine-grid error in the lift and aerodynamic-center pitching-moment coefficients was less than 0.5% of the mean values. The finite drag predicted by the CFD solutions and shown in Fig. 4 is due to *numerical viscosity* and results in a mean fine-grid drag-coefficient error of 0.00031 in this angles-of-attack range.

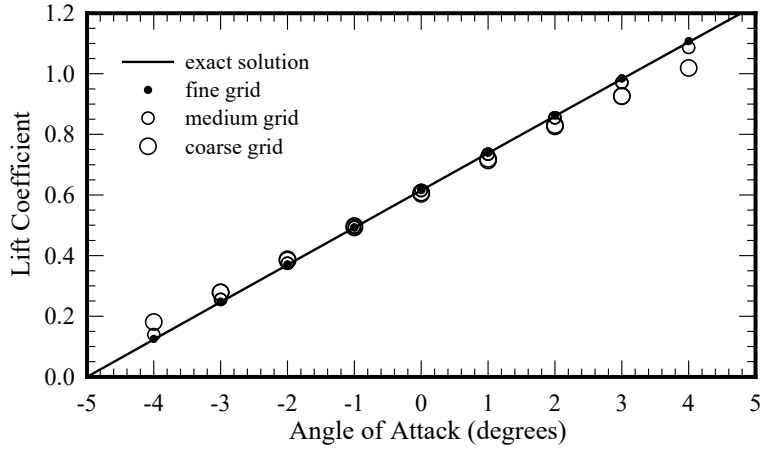

Figure 3. Coarse-, medium-, and fine-grid CFD solutions for the steady lift coefficient compared with the exact analytical solution.

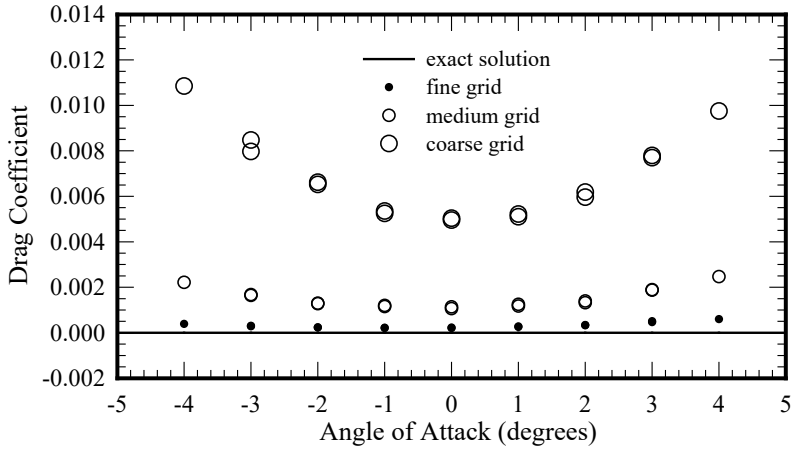

Figure 4. Coarse-, medium-, and fine-grid CFD solutions for the steady drag coefficient compared with the exact analytical solution.

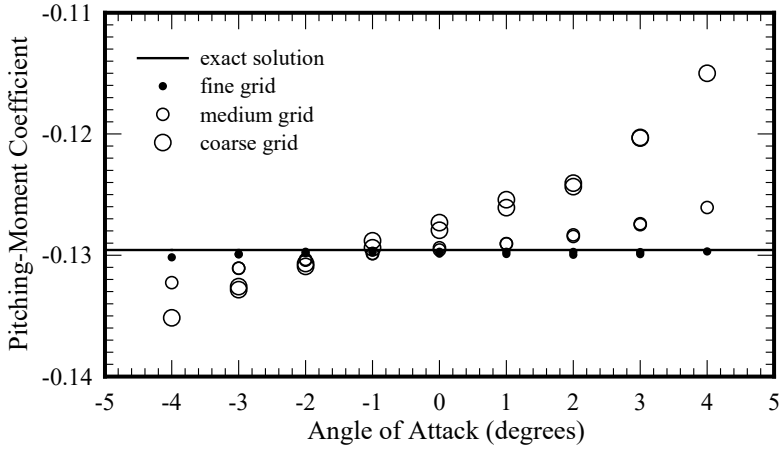

Figure 5. Coarse-, medium-, and fine-grid CFD solutions for the steady pitching-moment coefficient about the airfoil aerodynamic center compared with the exact analytical solution.

To ensure that the computational domain size was sufficient, the outer radius of the background C-grid was increased from 10 chord lengths to 20 chord lengths for a representative subset of cases with insignificant change in the results. Based on the results of this grid convergence study, the fine 561×121-node grid was used for all solutions presented here.

Typical axial reduced frequencies for birds in efficient forward flight range between $\hat{\omega}_x \cong 0.03$ for birds such as the wandering albatross to $\hat{\omega}_x \cong 0.4$ for birds such as the ruby-throated hummingbird. In order to prevent large numerical viscosity errors and the associated flow separation with inviscid CFD calculations, the geometric angle of attack must be typically limited to the range ± 6.0 degrees. Therefore, for all unsteady cases presented here, values for y_A, ω, and α_A were chosen such that the geometric angle of attack fell in the range $-5.37 < \alpha_g < 5.37$ degrees. This geometric-angle-of-attack constraint combined with the fact that the vertical displacement of the overset grid is limited resulted in a feasible reduced-frequency range of $0.1 < \hat{\omega}_x < 0.84$.

All transient CFD solutions were obtained using 128 time steps per cycle for eight cycles. The convergence criterion at each time step was set so that the difference in the *y*-momentum residual over 100 iterations was less than 10^{-8}. This criterion was set to 10^{-15} for a representative subset of cases with no significant change in the results. To assure that steady periodic solutions were obtained, the values of the axial force, normal force, and aerodynamic-center pitching moment at each time step during cycle eight were compared to the corresponding values during cycle seven. The maximum instantaneous deviation between the seventh and eighth cycle in percent of the mean ranged from 1.0×10^{-11}% to 2.6×10^{-2}% for the axial-force coefficient, from 3.0×10^{-12}% to 3.8×10^{-3}% for the normal-force coefficient, and from 2.3×10^{-12}% to 1.8×10^{-4}% for the aerodynamic-center pitching-moment coefficient. To assure that these CFD solutions were time-step converged, solutions were repeated using 256 time steps per cycle for a representative subset of the solutions. The mean deviation in the eighth cycle between the 128- and 256-time-step solutions ranged from 0.03% to 0.54% for the axial-force coefficient, from 0.0025% to 0.0055% for the normal-force coefficient, and from 0.0004% to 0.0046% for the aerodynamic-center pitching-moment coefficient.

From the analysis described above, it was concluded that the steady periodic CFD solutions obtained using the 561×121-node grid with 128 time steps per cycle for the duration of eight cycles were all grid and time-step converged. From each CFD solution, values were obtained for the mean axial-force coefficient and the mean required-power coefficient. These results were used with Eqs. (26) and (27) to evaluate the Fourier coefficients *A* and *B* for each of the CFD solutions.

Values for the Fourier coefficients *A* and *B* were obtained in this manner from a large number of CFD solutions. The axial reduced frequency $\hat{\omega}_x$ was varied from 0.10 to 0.84; the vertical reduced frequency $\hat{\omega}_y$ was varied from 0.025 to 0.117; and the pitching-to-plunging ratio $\hat{\alpha}_y$ was varied from -0.2 to 0.2. It was found that the values for

the Fourier coefficients A and B obtained from these CFD solutions could be correlated quite accurately using the following piecewise continuous functions:

$$A = (1+0.13\hat{\alpha}_y)\begin{cases} A_{15}\hat{\omega}_x^5 + A_{14}\hat{\omega}_x^4 + A_{13}\hat{\omega}_x^3 + A_{12}\hat{\omega}_x^2, & \hat{\omega}_x \le T_{A1} \\ A_{23}\hat{\omega}_x^3 + A_{22}\hat{\omega}_x^2 + A_{21}\hat{\omega}_x + A_{20}, & T_{A1} \le \hat{\omega}_x \le T_{A2} \\ A_{30} - A_{31}\exp(-A_{32}\hat{\omega}_x), & \hat{\omega}_x \ge T_{A2} \end{cases} \tag{28}$$

$$B = \{1-\exp[-(35.6-30.4\hat{\alpha}_y)\hat{\omega}_y]\}(1-0.71\hat{\alpha}_y^2)\begin{cases} B_{15}\hat{\omega}_x^5 + B_{14}\hat{\omega}_x^4 + B_{13}\hat{\omega}_x^3 + B_{12}\hat{\omega}_x^2, & \hat{\omega}_x \le T_{B1} \\ B_{23}\hat{\omega}_x^3 + B_{22}\hat{\omega}_x^2 + B_{21}\hat{\omega}_x + B_{20}, & T_{B1} \le \hat{\omega}_x \le T_{B2} \\ B_{30}, & \hat{\omega}_x \ge T_{B2} \end{cases} \tag{29}$$

The correlation coefficients in Eqs. (28) and (29) were determined by forcing continuity of the functions and their first derivatives at the transition points, while minimizing the RMS difference between the CFD solutions and the correlating functions. This produced the correlation coefficients given in Table 1. Using Eqs. (28) and (29) with the correlation coefficients given in Table 1 produces the results shown in Figs. 6 and 7.

Table 1. Correlation coefficients for Eqs. (28) and (29).

A_{15} =	97.29135	A_{23} =	0.546031	A_{30} =	0.587284	B_{15} =	–544.4944	B_{23} =	–14.76825	B_{30} =	–0.265167
A_{14} =	–43.97278	A_{22} =	–1.041703	A_{31} =	0.804087	B_{14} =	49.2633	B_{22} =	11.25173		
A_{13} =	–17.06888	A_{21} =	0.961984	A_{32} =	2.611038	B_{13} =	109.3024	B_{21} =	–2.75989		
A_{12} =	9.97222	A_{20} =	0.108206	T_{A1} =	0.332091	B_{12} =	–26.2319	B_{20} =	–0.05111	T_{B1} =	0.226322
				T_{A2} =	0.728294					T_{B2} =	0.300902

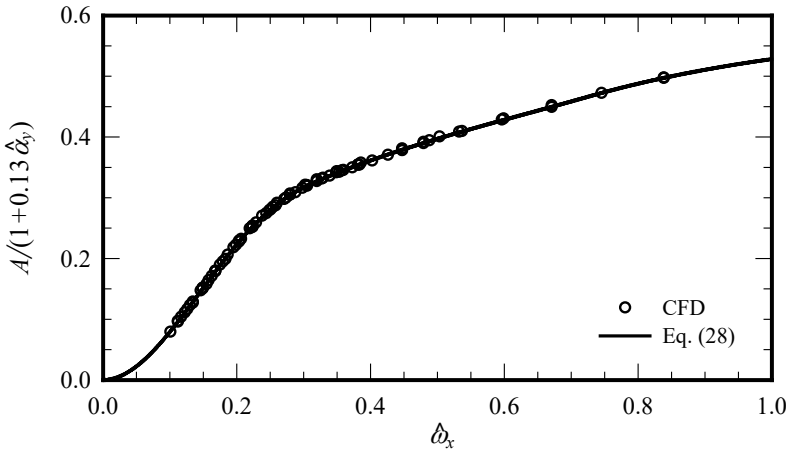

Figure 6. Comparison between the CFD solutions and the correlation with Eq. (28).

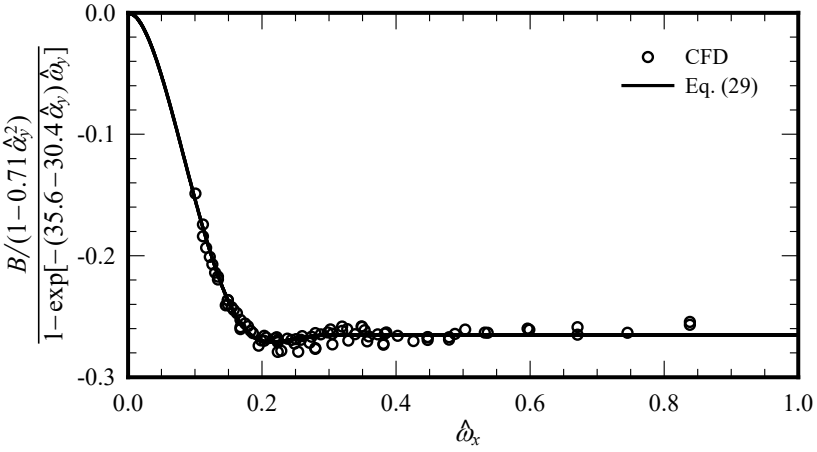

Figure 7. Comparison between the CFD solutions and the correlation with Eq. (29).

Note that Fig. 7 exhibits significantly more deviation between the CFD solutions and the correlation equation than does Fig. 6. This could be attributed to the fact that the relative uncertainty in the CFD solutions for the mean axial force is on the order of 3%, whereas that for the mean required power is less than 0.5%. These uncertainties were determined from results similar to those presented in Figs. 3 and 4.

Applying Eqs. (28) and (29) with the correlation coefficients given in Table 1 to Eqs. (17), (23), and (25) produces the results presented in Figs. 8–10, which are shown over the range of axial reduced frequencies that are typically encountered in the efficient forward flight of birds. All results shown in Figs. 8–10 were obtained for a geometric angle-of-attack amplitude of $\hat{\omega}_y(1-\hat{\alpha}_y) = 4.29°$ and a mean lift coefficient $\overline{C}_L = 0.614$. Results from the Theodorsen model are included for comparison. The deviation between the CFD results and Eqs. (17), (23), and (25) for all cases in this study ranges from –0.7% to 1.7% for the mean axial-force coefficient, from –0.08% to 0.6% for the mean required-power coefficient, and from –0.9% to 1.5% for the propulsive efficiency. Thus, in the range of reduced frequencies studied, the correlation matches the CFD results to within 2%. On the other hand, in the range of frequencies studied, the deviation between the CFD results and the model presented by Theodorsen [7] is from –2.9% to 34% for the mean axial-force coefficient, from –1.2% to 24% for the mean required-power coefficient, and from –2.4% to 8.3% for the propulsive efficiency. Because the CFD uncertainty in the mean axial-force coefficient is on the order of 3% and that for the mean required-power coefficient is on the order of 1%, we should expect the correlations presented here to provide a noticeable improvement over the Theodorsen model.

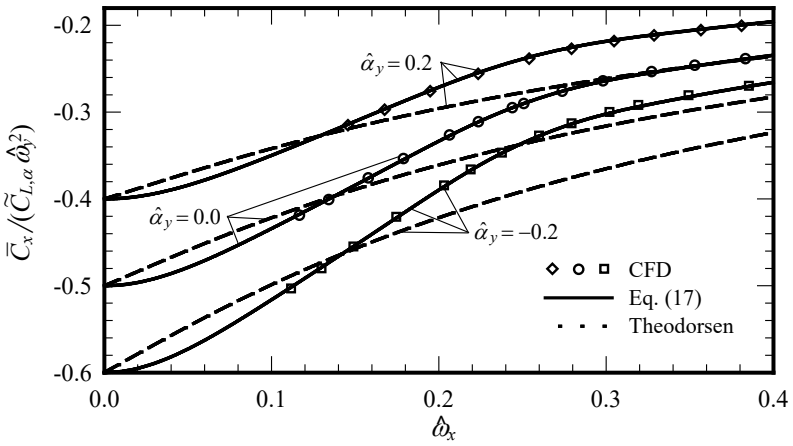

Figure 8. Comparison of the mean axial-force coefficient predicted from the CFD solutions, Eq. (17), and the model first presented by Theodorsen [7].

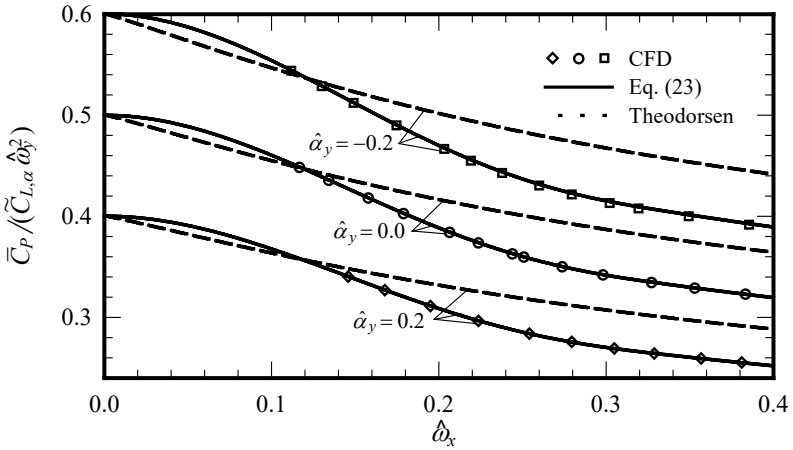

Figure 9. Comparison of the mean required-power coefficient predicted from the CFD solutions, Eq. (23), and the model first presented by Theodorsen [7].

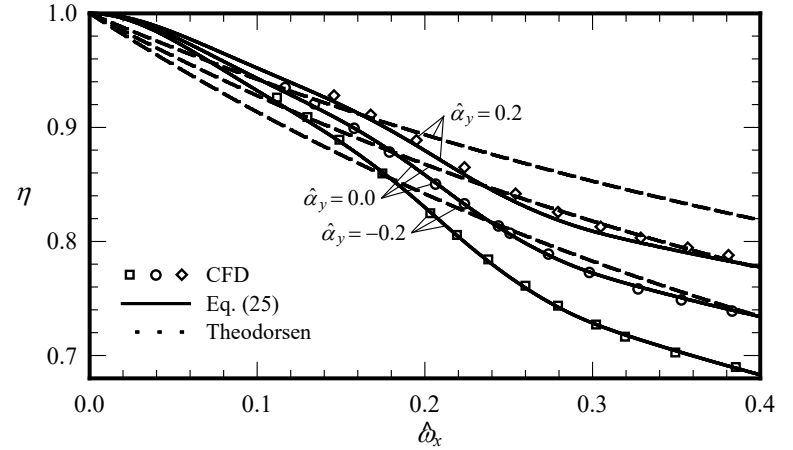

Figure 10. Comparison of the propulsive efficiency predicted from the CFD solutions, Eq. (25), and the model first presented by Theodorsen [7].

In order to obtain a closed-form solution, Theodorsen assumed a planar wake with sinusoidal oscillating vorticity. This assumption allowed him to evaluate the induced velocity on the airfoil due to the wake vorticity, and resulted in a wake model dependent on the axial reduced frequency, k [7,9]. However, because the wake model he developed was planar, he neglected the vertical oscillations within the wake due to the amplitude of the vertical oscillation of the airfoil, y_A (see Fig. 1). Thus, his wake model was independent of the normal reduced frequency, $\hat{\omega}_y$. At low reduced frequencies, when the freestream velocity is large compared to the product of the flapping frequency and the chord length, the wake moves downstream rapidly ($\lambda/c \to \infty$), and therefore the vertical oscillations in the wake are negligible. However, at high reduced frequencies, the effects of the vertical oscillations in the wake become more significant. Therefore, we would expect the Theodorsen model to give reasonable results at low frequencies, but we should not expect the Theodorsen model to be accurate at high frequencies.

In summary, Eqs. (28) and (29) along with the coefficients given in Table 1 can be used in Eqs. (17), (23), and (25) to predict the mean axial-force coefficient, required-power coefficient, and propulsive efficiency of airfoils in forward flight with sinusoidal pitching and plunging motion. Furthermore, the time-dependent induced angle of attack as well as the instantaneous force coefficients can be evaluated using Eqs. (13), (14), and (15) respectively. Because the model is written in terms of the airfoil aerodynamic coefficients $\widetilde{C}_{L,\alpha}$ and α_{L0}, this model can be used for any airfoil for which these coefficients are known, and is therefore not constrained to a specific airfoil. This model can be implemented over a wide range of flapping frequencies, amplitudes, and freestream airspeeds. However, the model does not apply to hovering or very low-speed flapping flight.

IV. Conclusions

It has been shown here that both axial and normal reduced frequencies are of significant importance in predicting the time-dependent aerodynamic forces acting on an airfoil undergoing sinusoidal flapping in forward flight. The axial reduced frequency is based on the chord length as defined in Eq. (21), and the normal reduced frequency is based on the aerodynamic-center plunging amplitude as defined in Eq. (5). Furthermore, it has been shown that the time-dependent aerodynamic forces can be related to only two Fourier coefficients. These Fourier coefficients were obtained in the present study from grid- and time-step-resolved inviscid CFD solutions, which encompass a range of flapping frequencies and amplitudes commonly encountered in the efficient forward flight of birds. The Fourier coefficients were found to be strong functions of the axial reduced frequency, $\hat{\omega}_x$, and weak functions of the normal reduced frequency, $\hat{\omega}_y$, and the geometric angle-of-attack ratio, $\hat{\alpha}_y$. Correlations for these Fourier coefficients were presented in Eqs. (28) and (29), which can be used with Eqs. (17), (23), and (25) to predict the mean axial-force coefficient, mean required-power coefficient, and mean propulsive efficiency for sinusoidal flapping of an airfoil with known geometry and known aerodynamic coefficients for steady flow. The algebraic

relations that are given in Eqs. (28) and (29) were correlated with the CFD results to obtain the correlation coefficients given in Table 1. Results obtained from the correlations presented in this paper match the CFD results to within 2.0% for the mean axial-force coefficient, mean required-power coefficient, and propulsive efficiency over the entire range of axial reduced frequencies studied.

Theodorsen's model has been compared to the CFD solutions in the range of flapping frequencies and amplitudes commonly encountered in the efficient forward flight of birds. The computational results agree reasonably well with the Theodorsen model at low flapping frequencies. In fact, for axial reduced frequencies in the range $\hat{\omega}_x < 0.2$, Theodorsen's model agrees with all CFD results from this study to within 10%. Even at higher frequencies, Theodorsen's model agrees with the numerical results to within 35%. This is rather remarkable considering the seemingly constraining approximations used by Theodorsen in developing the model. However, because the correlations provided in this paper were obtained from grid- and time-step-resolved CFD solutions, the present correlations can be used as an improvement over the model presented by Theodorsen [7] for predicting the propulsion of flapping airfoils in efficient forward flight.

References

[1] Knoller, R., "Die Gesetze des Luftwiderstandes," *Flug- und Motortechnik (Wien)*, Vol. 3, No. 21, 1909, pp. 1–7.

[2] Betz, A., "Ein Beitrag zur Erklärung des Segelfluges," *Zeitschrift für Flugtechnik und Motorluftschiffahrt*, Vol. 3, 1912, pp. 269–272.

[3] Katzmayr, R., "Effect of Periodic Changes of Angle of Attack on Behavior of Airfoils," NACA TR-147, Oct. 1922.

[4] Wagner, H. "Über die Entstehung des dynamischen Auftriebs von Tragflügeln," *Zeitschrift für Angewandte Mathematic und Mechanik*, Vol. 5, No. 1, Feb. 1925, pp. 17–35.

[5] Glauert, H., "The Force and Moment on an Oscillating Aerofoil," *Technical Report of the Aeronautical Research Committee*, Vol. 2, R. & M. No. 1242, 1931, pp. 742–758.

[6] von Kármán, T., and Burgers, J. M., "General Aerodynamic Theory — Perfect Fluids," *Aerodynamic Theory*, edited by Durand, W. F., Vol. 2, Springer, Berlin, 1935, pp. 293–310.

[7] Theodorsen, T., "General Theory of Aerodynamic Instability and the Mechanism of Flutter," NACA TR-496, Feb. 1935.

[8] Garrick, I. E., "Propulsion of a Flapping and Oscillating Airfoil," NACA TR-567, May 1936.

[9] Hunsaker, D. F., and Phillips, W. F., "Propulsion Theory of Flapping Airfoils, Comparison with Computational Fluid Dynamics," 53rd AIAA Aerospace Sciences Meeting, 5–9 January 2015, Kissimmee, Florida, AIAA-2015-0257.

[10] Anderson, J. M., Streitlien, K., Barrett, D. S., and Triantafyllou M. S., "Oscillating Foils of High Propulsive Efficiency," *Journal of Fluid Mechanics*, Vol. 360, Apr. 1998, pp. 41–72.

[11] Heathcote, S. and Gursul, I., "Flexible Flapping Airfoil Propulsion at Low Reynolds Numbers," *AIAA Journal*, Vol. 45, No. 5, 2007, pp. 1066–1079.

[12] Gulcat, U., "Propulsive Force of a Flexible Flapping Thin Airfoil," *Journal of Aircraft*, Vol. 46, No. 2, 2009, pp. 465–473.

[13] Ramesh, K., Gopalarathnam, A., Granlund, K., Ol, M. V., and Edwards, J. R., "Discrete-Vortex Method with Novel Shedding Criterion for Unsteady Aerofoil Flows with Intermittent Leading-Edge Vortex Shedding," *Journal of Fluid Mechanics*, Vol. 751, July 2014, pp. 500–538.

[14] Tuncer, I., and Kaya, M., "Optimization of Flapping Airfoils for Maximum Thrust and Propulsive Efficiency," *AIAA Journal*, Vol. 43, No. 11, 2005, pp. 2329–2336.

[15] Young, J. and Lai, J. C. S., "Mechanisms Influencing the Efficiency of Oscillating Airfoil Propulsion," *AIAA Journal*, Vol. 45, No. 7, 2007, pp. 1695–1702.

[16] Baik, Y. S., Bernal, L. P., Granlund, K., and Ol, M. V., "Unsteady Force Generation and Vortex Dynamics of Pitching and Plunging Aerofoils," *Journal of Fluid Mechanics*, Vol. 709, Oct. 2012, pp. 37–68.

[17] Brunton, S. L., Rowley, C. W., and Williams, D. R., "Reduced-Order Unsteady Aerodynamic Models at Low Reynolds Numbers," *Journal of Fluid Mechanics*, Vol. 724, June 2013, pp. 203–233.

[18] CD-adapco, "User Guide: Star-CCM+ Version 8.06," 2013, pp. 1–13268.

[19] Karamcheti, K., *Principles of Ideal-Fluid Aerodynamics*, Wiley, New York, 1966.

[20] Phillips, W. F., Fugal, S. R., and Spall, R. E., "Minimizing Induced Drag with Wing Twist, Computational-Fluid-Dynamics Validation," *Journal of Aircraft*, Vol. 43, No. 2, 2006, pp. 437–444.